Influence of crack morphology on creep-stage modelling of 316L(N) austenitic stainless steels

Oguz Berk Ozdemir[a*]

[a]Hacettepe University, Faculty of Engineering, Department of Nuclear Energy Engineering, Ankara, Türkiye

*oguzberkozdemir@hacettepe.edu.tr

(Received 07 May 2026; Accepted 28 July 2026)

Abstract

The creep behaviour of a reference 316L(N) grade and a modified 316L(N) grade with adjusted minor alloying elements, mainly N, Nb, and B (Steel A), was investigated at 575 °C and 310 MPa. The strain–time response was analysed across primary, steady-state, and tertiary creep stages. Steel A exhibited a rupture life of 9203 h, compared with 649 h for the reference steel. Optical microscopy, SEM, and X-ray tomography revealed narrow wedge-type cracks in the reference steel, whereas Steel A developed thicker and more rounded R-type cracks. The Estrin–Mecking approach described the primary and steady-state stages, while Ganesan's damage-tolerance factor and Yin's cavity-growth model were used for the tertiary stage. The damage-tolerance parameter λ increased from 3.6 to 4.6. In the Estrin–Mecking analysis, the fitted internal-stress parameters increased from 215 to 239 MPa for the reference steel and from 230 to 253 MPa for Steel A. These results suggest that crack morphology should be considered when interpreting tertiary creep model parameters, particularly when models are based on different damage assumptions.

Keywords

316 L(N) stainless steel; creep modelling; crack morphology; creep stages; internal stress; damage tolerance factor (λ)

1. Introduction

Austenitic stainless-steel grade 316 L(N), designated as Alloy 1S in the RCC-MRx code, has long been known for its critical role in high-temperature applications [1]. Drawing on operational experience from earlier French sodium-cooled fast reactors (SFRs), this alloy was developed to meet the service demands in primary sodium environments, including reactor vessels, primary circuit structures, core cover plugs, and intermediate heat exchangers [2] [3] [4]. In Generation IV nuclear power plant (NPP) concepts, this grade remains under consideration for parts expected to operate for 60 years without replacement [3]. For components in hot collector regions, where service temperatures may approach 550 °C and mechanical loading is moderate, the alloy is required to withstand prolonged thermal ageing while preserving creep strength, resistance to creep–fatigue, and adequate ductility and tensile capacity over its lifetime [3] [4]. In SFR systems, areas above the reactor core, the accumulated neutron dose is predicted to stay below roughly 1 displacement per atom (dpa), placing such regions in the low-dose irradiation category [3]. In these conditions, degradation is driven primarily by thermally activated processes, with creep and creep–fatigue emerging as the dominant long-term damage mechanisms [2] [5] [6] .

The RCC-MRx design code provides the framework for qualifying materials and designing structural components for high-temperature nuclear systems, including sodium-cooled fast reactors, by incorporating feedback from research programs, manufacturing practice, and operational service experience. Within this code, austenitic stainless steel 316 L(N) is specified with defined limits for chemical composition and mechanical performance to ensure its suitability in elevated-temperature service [1]. Numerous studies have investigated the influence of nitrogen variation on the creep behaviour [7] [8] [9] [10] [11] . The addition of nitrogen has been reported to improve rupture life by lowering the stacking-fault energy, which influences precipitation kinetics, delays the onset of initial precipitation, and reduces the diffusion of carbon and chromium [7]. In addition to nitrogen optimization, ongoing R&D programs have refined the control of niobium, boron, and carbon to achieve optimal phase stability, suppress ageing-related embrittlement, and provide reliable mechanical performance under long-term high-temperature operation [12] [13] [14] [15] [16] [17]. Small additions of niobium form stable Nb(C,N) precipitates when kept below the solubility limit for the given carbon level, but higher amounts offer no further benefit [13] [18]. Boron is one of the most challenging elements to characterize due to its low atomic number, and instead of conventional methods such as SEM, advanced techniques like Atom Probe Tomography (APT) or Secondary Ion Mass Spectrometry (SIMS) are required to detect it within the matrix [15] [16] [17]. Despite these challenges, boron has been associated with grain boundary strengthening and improvements in rupture life, particularly under low-stress conditions [16].

In nuclear systems, where replacement of primary circuit structures is impractical, accurate prediction of creep lifetime is essential for ensuring structural integrity during decades of operation. Numerous approaches have been applied to model the creep behaviour of 316 L(N), ranging from empirical fits of design code data to more mechanistic descriptions that incorporate deformation stages and microstructural evolution [19] [20] [21] [22] [23] [24] [25]. Various phenomenological models have been proposed to represent the complete creep curve by separately treating the primary, secondary, and tertiary stages [20] [21]. Primary and steady-state regions are often described through hardening–recovery frameworks such as the Estrin–Mecking model [24], which links internal stress evolution to strain rate behaviour. The tertiary stage, where damage accumulation accelerates until rupture, has been addressed through cavity growth or damage-tolerance-based descriptions, as seen in the works of Ganesan and Yin [19] [22]. These approaches have demonstrated the ability to reproduce experimental strain–time trends under a range of stresses and temperatures, providing valuable tools for interpreting microstructural observations and for predicting the remaining life of critical components.

Although the beneficial influence of minor alloying additions on the creep resistance of 316L(N)-type stainless steels has been widely discussed, this influence has generally been evaluated through rupture life, creep rate, precipitation behaviour, or post-mortem damage observations [2] [5] [6] [7]

[14]. Several constitutive approaches have also been proposed to reproduce the primary, steady-state, and tertiary stages of creep in 316L(N) and related austenitic stainless steels [19] [20] [21] [22] [24]. However, the link between the observed crack morphology and the interpretation of creep-stage model parameters remains less clearly established. This is especially relevant for compositionally close 316L(N) steels tested under the same temperature and stress, where acceptable numerical agreement with the creep curve may still correspond to different underlying damage mechanisms.

In the present study, the creep behaviour of a 316L(N) stainless steel grade conforming to the RCC-MRx specification and a modified grade produced with slight adjustments in nitrogen, boron, and niobium contents was analysed. Both steels were tested at 575 °C under 310 MPa, a condition also relevant to recent comparative studies on 316L(N)-type alloys with different microstructural states [26]. Previous investigations on the present materials, based on SEM, TEM, EBSD, phase analysis, and X-ray tomography, showed marked differences in precipitation sequence and creep damage morphology [5] [6] . Building on these observations, the present work does not aim to isolate the individual contribution of each alloying element. Instead, it combines stage-wise creep modelling with three-dimensional damage observations in order to examine how the macroscopic creep response and the observed crack morphology should be interpreted together for two compositionally close 316L(N) steels tested under identical creep conditions.

2. Experimental Details

The chemical compositions of the investigated materials are summarized in Table 1. The first material was a 316 L(N) stainless steel grade conforming to the RCC-MRx-2018 specification and is referred to here as the reference steel [1]. The second material was a modified 316 L(N) grade, referred to as Steel A, in which the nitrogen, boron, and niobium contents were adjusted. Both alloys were produced within the RCC-MRx material concept in order to examine the influence of minor compositional changes on creep behaviour. The reference steel was solution annealed at 1085 °C for one hour, while Steel A was annealed at 1100 °C for the same duration [2]. Plates were hot rolled with cross-rolling passes to final thicknesses of 30 mm for the reference steel and 40 mm for Steel A, followed by water quenching. In both materials, a small amount of retained ferrite (< 1 %) was present along the rolling direction [2].

Table 1 : Chemical compositions of the reference steel and Steel A, with the RCC-MRx-2018 specification for comparison. Values are given in wt.% unless otherwise stated.

Designation	C	Si	Mn	P	S	Cr	Ni	Cu	Mo	Co	Nb	B	N
RCC-MR$_{x-2018}$	≤0.03	≤0.5	1.60 2.00	≤0.03	≤0.015	17.00 18.00	12.00 12.50	≤1.00	2.30 2.70	<0.2	-	≤20 ppm	0.06 0.08
Reference Steel	0.03	0.39	1.84	0.028	<0.003	17.3	12.5	0.17	2.48	0.13	0.014	11	0.075
Steel A	0.021	0.42	1.71	0.021	0.0018	17.7	12.6	0.06	2.46	0.03	0.09	19	0.1

Creep specimens were machined with a gauge length of 38 mm and a diameter of 5 mm. The specimen axis was parallel to the rolling plane defined by the two main rolling directions. In this orientation, the elongated ferrite plates were aligned parallel to the tensile axis of the creep specimen [2]. All creep tests were performed at the EDF R&D laboratory under a nominal stress of 310 MPa at a temperature of 575 °C, in accordance with the EN-ISO-204/2009 standard procedure [5] [6]. During testing, elongation was continuously recorded using displacement gauges mounted on the lever arms and connected to an automated data acquisition system.

For the creep-stage modelling presented in this work, the strain–time curves obtained from the two full creep-rupture tests were used as the main input data. These tests correspond to one ruptured specimen for the reference steel and one ruptured specimen for Steel A. In addition to these full rupture tests, destructive interrupted creep tests were performed under the same temperature and stress conditions. Six destructive interrupted creep specimens, three for each steel, were used for microstructural and damage characterization at selected creep strain levels. These interrupted tests were used to check the consistency of the creep-stage evolution and to support the interpretation of damage development. Detailed experimental information on the destructive interrupted creep tests has been reported previously [6].

Microstructural observations were performed on both the reference steel and Steel A in the as-received condition and after creep rupture. Optical microscopy (OM) was carried out using an Olympus DSX510 to examine the as-received and fractured specimens, while scanning electron microscopy (SEM) analyses were conducted using a FEG-Jeol IT500HR microscope in secondary electron and electron backscatter diffraction modes. Observations on ruptured samples were performed in gauge-section regions that were also investigated by tomography, allowing destructive and non-destructive observations to be compared. High-resolution X-ray tomography was performed on selected regions of ruptured creep specimens using an EASYTOM XL system with a laboratory X-ray source. The scans were acquired at a resolution of 0.65 μm per pixel, with 1440 projections over 360°. Volume reconstruction was performed using Xact software and a classical back-projection algorithm [27]. Each dataset covered a total volume of 0.061 mm^3. The same acquisition, reconstruction, and segmentation approach was used for both steels, allowing a direct comparison of local crack and cavity morphology under identical analysis conditions. This volume was used to resolve individual damage features in three dimensions and to complement the OM and SEM observations.

3. Results and Discussion

3.1. Creep test results

The creep performance of the reference steel and Steel A was assessed at 575 °C under a constant applied stress of 310 MPa. The full creep-rupture curves are presented in Figure 1 together with the final interruption points of the destructive interrupted creep tests performed under the same testing conditions. The symbols in Figure 1 correspond to the last recorded strain–time point of each interrupted specimen before interruption. Detailed strain and time information for the destructive interrupted creep tests has been reported previously [6]. For both steels, these points fall on the same overall strain–time response as the corresponding full creep-rupture curves, indicating that the interrupted specimens followed a consistent creep evolution before being stopped for microstructural and damage characterization. Since the interrupted specimens were stopped before rupture, they are not included in Table 2 as rupture-property data. The rupture properties obtained from the two full creep-rupture tests are summarized in Table 2.

Under the same test conditions, Steel A exhibited a rupture life of 9203 h, compared with 649 h for the reference steel. Although the difference between the two steels is based on relatively small changes in chemical composition, Steel A exhibited approximately fourteen times longer rupture life than the reference steel. In addition, Steel A showed higher elongation and necking values. This indicates that the improvement in rupture life was not obtained at the expense of macroscopic ductility. This large difference in rupture behaviour is therefore considered together with the damage observations and creep-stage modelling results discussed in the following sections.

Table 2 : Creep test conditions and results for the reference steel and Steel A

Steel identification	Temperature (°C)	Stress (MPa)	Time to Rupture (hr)	Elongation (%)	Necking (%)
Reference Steel	575	310	649	18.8	29.5
Steel A	575	310	9203	22.8	39.5

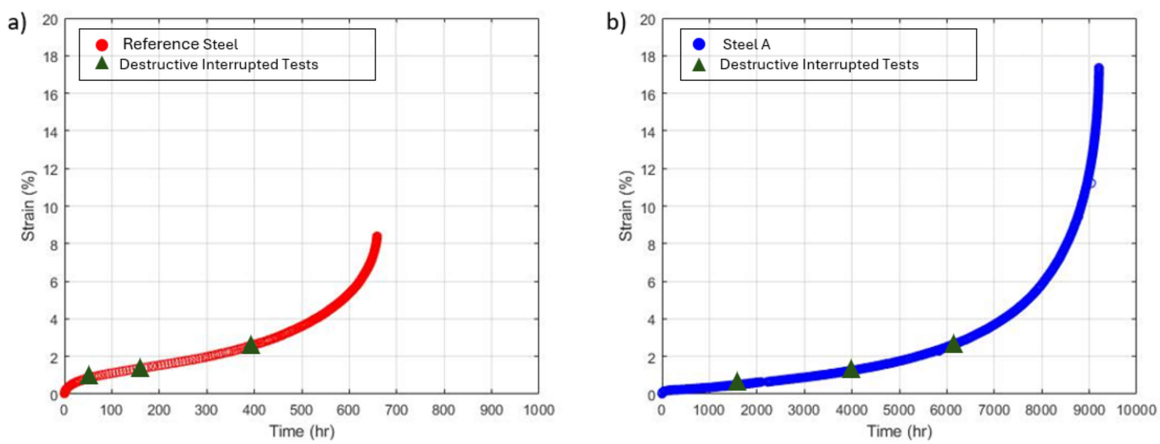

Figure 1 : Strain–time creep response of (a) the reference steel and (b) Steel A at 575 °C and 310 MPa. The full creep-rupture curves are shown together with the final interruption points of the destructive interrupted creep tests performed under the same testing conditions.

3.2. Microstructural analysis of creep damage

Regions near the main fracture surface, where extensive crack coalescence occurred, were examined in both steels. Representative optical microscopy, SEM, and three-dimensional X-ray tomography observations are presented in Figure 2. These observations show that the two materials developed clearly different crack morphologies after creep rupture. In the reference steel, cracks were generally narrow, elongated, and frequently aligned along grain boundaries. This morphology is consistent with wedge-type cracking, as described in the literature [22]. In Steel A, cracks of comparable length appear thicker and more rounded, corresponding to the R-type classification and indicating a different damage-growth mechanism [22].

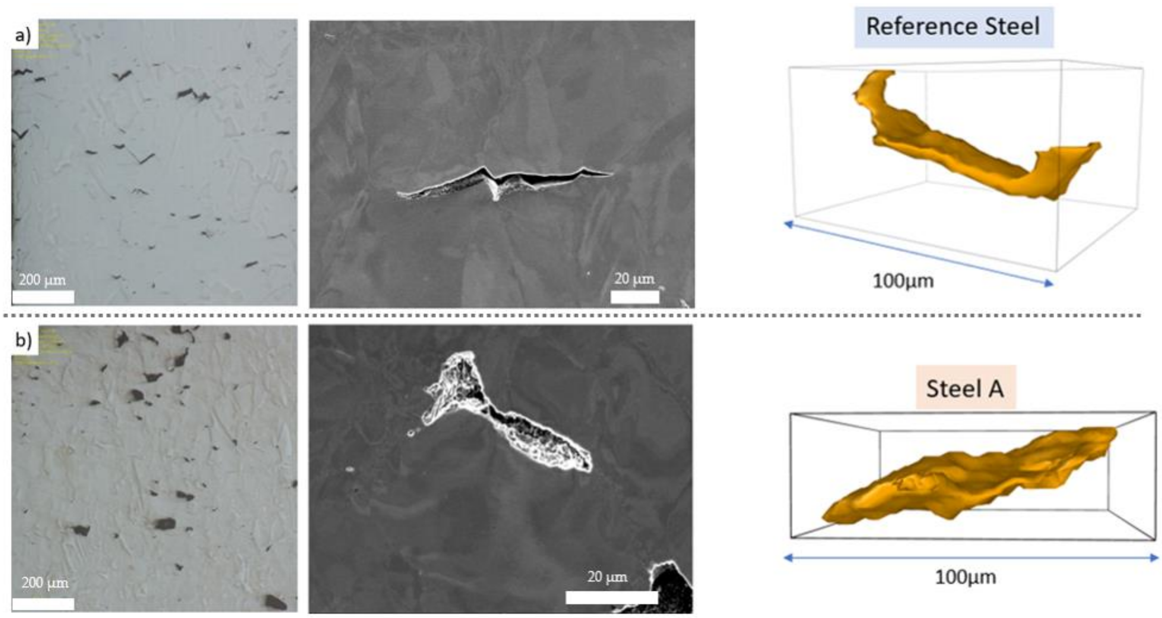

Figure 2 : OM, SEM, and 3D X-ray tomography observations of crack morphology near the fracture region in (a) the reference steel and (b) Steel A. The left, middle, and right columns correspond to OM, SEM, and 3D tomography observations, respectively. Scale bars are provided to allow comparison of the characteristic damage features observed in each technique.

The three-dimensional tomography observations should be interpreted together with the OM and SEM results, since the analysed volume provides a local comparison of damage morphology under identical imaging and segmentation conditions. The SEM images are used as representative observations of the dominant crack morphology in each steel, and the scale bars allow the relative size of the observed damage features to be assessed. Within this volume, the reference steel showed narrow and elongated crack features consistent with wedge-type cracking, whereas Steel A showed thicker and more rounded crack features corresponding to R-type morphology. This trend is consistent with the previously reported quantitative three-dimensional crack-thickness analysis performed on the same material system, where the maximum local thickness distribution showed finer crack features in the reference steel and thicker crack features in Steel A [6]. In both alloys, damage is concentrated along grain boundaries; however, the contrasting crack morphologies suggest that the modified composition affects the damage-development path during creep. As noted in a previous study [6], the higher nitrogen level in Steel A was associated with modified precipitation behaviour, while the combined presence of boron and niobium may contribute to microstructural stabilization. A recent study on Nb-free and Nb-rich 316L(N) steels tested under the same creep condition, 575 °C and 310 MPa, also showed that Nb-containing material can exhibit a different creep-damage response and longer creep lifetime [26]. However, the individual contributions of N, Nb, and B cannot be isolated in the present alloy because these elements, together with C, were modified simultaneously. Therefore, the difference in crack morphology should be interpreted as the result of combined minor compositional modifications rather than the effect of a single alloying element. Taken together with the creep data in Table 2, this difference in damage morphology provides a microstructural basis for interpreting the approximately fourteen-fold longer rupture life of Steel A and motivates the subsequent creep-stage modelling analysis.

3.3. Modelling of creep stages

The modelling work was carried out by treating the primary, steady-state, and tertiary creep stages separately. This approach was selected because each stage is controlled by different deformation and damage processes. The primary and steady-state stages were modelled using the Estrin–Mecking framework, whereas the tertiary stage was analysed using both the damage-tolerance approach proposed by Ganesan and the cavity-growth-based formulation proposed by Yin [19] [22] [24].

These models were selected because they allow a stage-wise interpretation of the creep response together with the observed damage morphology. Other approaches, including the θ-projection method, the Norton–Bailey law, and Kachanov–Rabotnov-type damage models, are useful for creep-curve reproduction or lifetime prediction; however, the present work focuses on comparing creep-stage behaviour with wedge-type and R-type crack morphologies.

Primary and steady-State creep stage

The primary and steady-state creep behaviour of both steels was modelled using the Estrin–Mecking framework [24], which relates the evolution of internal stress to the accumulated strain. This approach was previously applied to 316 L(N) stainless steels with different nitrogen contents by Praveen [20], and a similar methodology was adopted in the present work to describe internal stress evolution. The strain-dependent form of the model is expressed as:

$$\frac{d\sigma_i}{d\varepsilon} = \frac{1}{\sigma_i \varepsilon_c}\left(\sigma_{is}^2 - \sigma_i^2\right) \qquad \text{Equation 1}$$

Where σ_i is the internal stress, σ_{is} is the saturation internal stress, and ε_c is characteristic strain for internal stress saturation. The time-dependent form of the model is obtained by combining the Equation 1 with the strain rate, $\dot{\varepsilon}$, leading to:

$$\frac{d\sigma_i}{dt} = \frac{1}{\sigma_i \varepsilon_c}\left(\sigma_{is}^2 - \sigma_i^2\right)\dot{\varepsilon} \qquad \text{Equation 2}$$

Strain rate,$\dot{\varepsilon}$, is defined according to Equation 3, which incorporates parameters related to dislocation dynamics and diffusion processes:

$$\dot{\varepsilon} = \frac{\rho_m b^2 \upsilon_D \sigma_e\left(\sigma_i^2 \sigma_e\right)}{M^2} esp\left(\frac{-Q}{RT}\right) sinh\left(\frac{\sigma_e}{MkT} b^3 \left[\frac{\mu}{\left(\sigma_i^2 \sigma_e\right)^{1/3}}\right]\right) \qquad \text{Equation 3}$$

In this expression, ρ_m is mobile dislocation density, b is scalar value of Burgers vector, υ_D is Debye frequency, σ_e is effective stress, M is material constant, Q is the activation energy for lattice diffusion of Fe in γ iron, R is constant, T is temperature, k is Boltzmann constant, μ is shear modulus. By combining the Equation 1 and Equation 3, the evolution of internal stress as a function of time can be described for both the primary and steady-state creep stages.

The material constants used in the model were taken from the literature [20] and are summarized in Table 3, while the internal stress parameters reported in Table 4 were obtained by fitting the model to the experimental creep curves. These values should therefore be interpreted as model-derived internal-stress parameters rather than direct experimental measurements of internal stress. Numerical integration was carried out using a fourth-order Runge–Kutta method. The model successfully reproduced the experimental strain–time behaviour of both steels, as illustrated in Figure 3.

Table 3 : Material parameters used in modelling [20]

Constant	B	Q	K	M	μ	R	υ_D	ρ_m
Unit	M	$kJmol^{-1}$	JK^{-1}	-	MPa	$Jmol^{-1}K^{-1}$	h^{-1}	m^{-2}
Value	$0.258x10^{-9}$	285	$1.38x10^{-23}$	3.0	57301.9	8.314	$3.6x10^{16}$	$5x10^{11}$

Table 4 : Fitted internal stress parameters obtained from the Estrin-Mecking model

Fitted internal-stress parameter	Reference Steel	Steel A
σ_i (MPa)	215	230
σ_{is} (MPa)	239	253

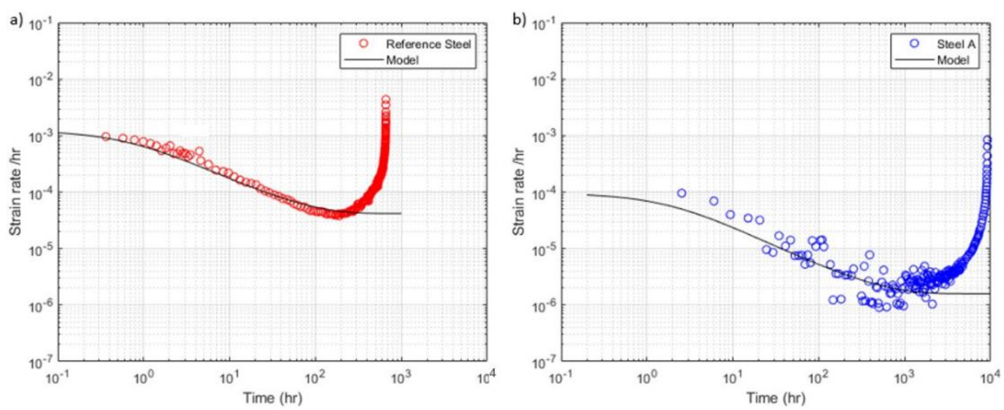

Figure 3 : Comparison between experimental and calculated strain-rate evolution for (a) the reference steel and (b) Steel A at 575 °C and 310 MPa using the Estrin–Mecking model.

Figure 3(a) and Figure 3(b) show that the calculated strain-rate curves reproduce the experimental strain-rate evolution of both the reference steel and Steel A in the primary-to-minimum creep-rate range. The experimental strain-rate curves show that the minimum creep rate was approximately $4\,x\,10^{-5}\,h^{-1}$for the reference steel and approximately $2\,x\,10^{-6}\,h^{-1}$ for Steel A. This lower minimum creep rate is consistent with the longer rupture life of Steel A. The validation metrics in Table 6 further support this agreement. This indicates that the difference between the two steels can be reasonably represented through changes in the internal stress evolution parameters.

Throughout the entire creep test, the calculated internal stress of Steel A remained higher than that of the reference steel, as presented in Figure 4. This result is consistent with the improved creep resistance of the modified alloy. Praveen [21] reported that increasing nitrogen content from 0.07 wt.% to 0.11 wt.% produced an internal stress increase of about 5 MPa. In the present study, the difference between the reference steel and Steel A was larger, approximately 20 MPa. This larger difference should not be attributed to nitrogen alone; rather, it likely reflects the combined influence of nitrogen, niobium, and boron on dislocation motion, precipitation behaviour, and grain-boundary stability. Although the individual contribution of each element cannot be separated in the present analysis, the fitted parameters indicate that the modified composition enhances the resistance of Steel A to creep deformation.

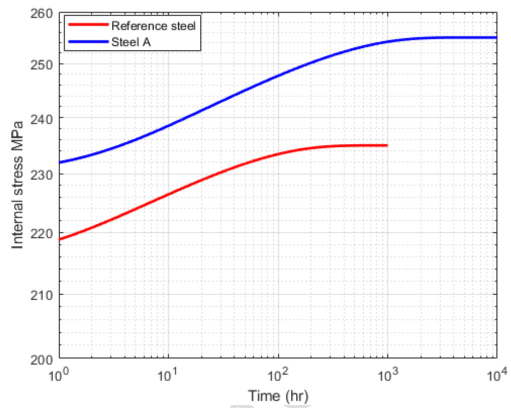

Figure 4 : Evolution of calculated internal stress as a function of time for the reference steel and Steel A during creep testing at 575 °C under 310 MPa.

Tertiary creep stage

The tertiary creep stage was first analysed using the damage-tolerance model proposed by Ganesan [19] for 316LN. This method uses the damage-tolerance factor, λ, originally introduced by Ashby and Dyson [25], to describe the contribution of tertiary creep to the total deformation before rupture. It is defined as:

$$\lambda = \frac{\varepsilon_f}{\dot{\varepsilon}_s t_r} \qquad \text{Equation 4}$$

Where t_r is the rupture time, ε_f is the elongation at fracture, and $\dot{\varepsilon}_s$ is the steady state creep rate. In the present study, λ was calculated as 3.6 for reference steel and 4.6 for steel A. These values indicate that the contribution of tertiary creep to the total deformation differs between the two steels, even though both materials belong to the same 316 L(N) alloy family. The difference in λ is consistent with the difference in crack morphology observed after creep testing. Using λ, the strain rate–time relationship can be expressed as [19]:

$$\dot{\varepsilon} = \dot{\varepsilon}_s \left(1 - \frac{t}{t_r}\right)^{\frac{1}{\lambda}-1} \qquad \text{Equation 5}$$

The strain-rate evolution predicted by the damage-tolerance approach showed good agreement with the experimental data for both steels, as shown in Figure 5. This suggests that the model can effectively describe the acceleration of creep rate during the tertiary stage when the damage evolution is represented in an averaged form. However, this approach does not explicitly distinguish between different crack morphologies. Therefore, while the model is useful for reproducing the global strain-rate trend, it provides limited information about why the reference steel and Steel A develop different damage structures.

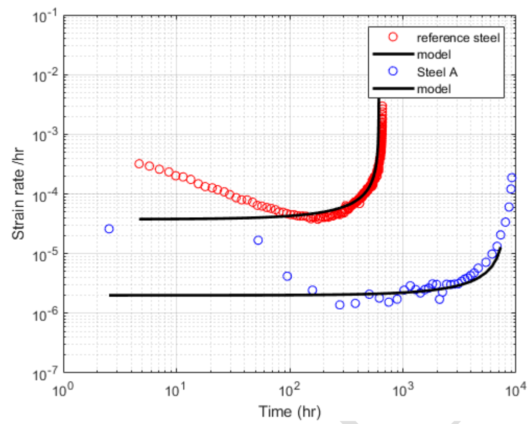

Figure 5 : Experimental and calculated strain-rate evolution in the tertiary creep stage for the reference steel and Steel A using the Ganesan damage-tolerance model.

A second analysis was performed using the cavity-growth-based damage formulation proposed by Yin [22]. In this approach, the strain rate is expressed as a function of time by coupling the dislocation-creep relation with an internal damage variable, w, representing the progressive reduction in effective load-bearing area caused by cavity formation and growth. The constitutive relation used in the present study is given by:

$$\dot{\varepsilon} = \frac{\rho_m b^2 \upsilon_D \sigma_e (\sigma_i^2 \sigma_e)}{M^2} esp\left(\frac{-Q}{RT}\right) sinh\left(\frac{\sigma_e}{MkT(1-w)} b^3 \left[\frac{\mu}{\left(\sigma_i^2 \sigma_e\right)^{1/3}}\right]\right) \qquad \text{Equation 6}$$

The associated damage evolution law is defined as:

$$\frac{dw}{dt} = K\varepsilon^m \dot{\varepsilon} \qquad \text{Equation 7}$$

where K and m are the fitting parameters of the model. These coupled equations were solved numerically using a fourth-order Runge–Kutta method, and the fitting parameters were adjusted separately for the two steels, as summarized in Table 5. The comparison between the experimental and calculated strain-rate evolution is presented in Figure 6.

Table 5 : Fitting parameters used in the Yin cavity-growth model

Fitting Parameters	Reference Steel	Steel A
σ_i (MPa)	215	230
σ_{is} (MPa)	239	253
ε_c	0.009	0.001
K	3.77	4.09
m	0.002	0.00004

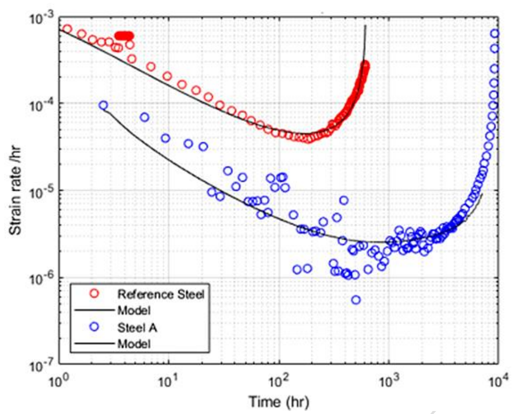

Figure 6 : Experimental and calculated strain-rate evolution obtained using the Yin cavity-growth model for the reference steel and Steel A at 575 °C and 310 MPa.

To provide a quantitative assessment of the model predictions, the agreement between the experimental and calculated strain-rate curves was evaluated using the root mean square error (RMSE), mean absolute error (MAE), and coefficient of determination (R^2). The metrics were calculated within the creep-stage range for which each model was applied. For the Estrin–Mecking model, the comparison was restricted to the primary-to-minimum creep-rate range, whereas the Ganesan damage-tolerance and Yin cavity-growth models were evaluated in the tertiary creep stage. The resulting values are summarized in Table 6.

Table 6 : Quantitative validation metrics for the creep-stage models. RMSE, MAE, and R^2 were calculated using the experimental and calculated strain-rate values at the same time points.

Model	Steel identification	Analysed creep-stage range	RMSE(h^{-1})	MAE(h^{-1})	R^2
Estrin-Mecking model	Reference Steel	Primary-to-minimum creep-rate range	$1.47\ x\ 10^{-5}$	$9.36\ x\ 10^{-6}$	0.943
Estrin-Mecking model	Steel A	Primary-to-minimum creep-rate range	$5\ x\ 10^{-6}$	$2.17\ x\ 10^{-6}$	0.664
Ganesan damage-tolerance model	Reference Steel	Tertiary creep stage	$6.7\ x\ 10^{-5}$	$4.35\ x\ 10^{-5}$	0.849
Ganesan damage-tolerance model	Steel A	Tertiary creep stage	$1.71\ x\ 10^{-5}$	$8.68\ x\ 10^{-6}$	0.682
Yin cavity-growth model	Reference Steel	Tertiary creep stage	$1.27\ x\ 10^{-5}$	$9.96\ x\ 10^{-6}$	0.902
Yin cavity-growth model	Steel A	Tertiary creep stage	$8.81\ x\ 10^{-7}$	$5.99\ x\ 10^{-7}$	0.900

The analysed time ranges were 5–300 h and 5–2600 h for the Estrin–Mecking model in the reference steel and Steel A, respectively; 300–649 h and 2600–9203 h for the Ganesan damage-tolerance model; and 300–619 h and 2600–9203 h for the Yin cavity-growth model.

The validation metrics indicate that the Estrin–Mecking model provides a good description of the primary-to-minimum creep-rate range, particularly for the reference steel. In the tertiary stage, the Ganesan damage-tolerance model gives reasonable agreement for both steels and provides a useful comparative parameter through λ. The highest R^2 values in the tertiary stage were obtained with the Yin cavity-growth model, with R^2 values of 0.902 for the reference steel and 0.900 for Steel A. This indicates that the Yin model provides the closest quantitative description of the analysed tertiary strain-rate evolution.

The difference in model interpretation can be linked to the observed crack morphology. Yin's formulation is more directly compatible with wedge-type damage development, which was the dominant morphology in the reference steel. In contrast, Steel A mainly exhibited thicker and more rounded R-type cracks. Although the Yin model also provides close numerical agreement for Steel A, this morphology is less directly represented by a classical cavity-growth formulation. Thus, the modelling results suggest that tertiary creep models should not be evaluated only by their numerical fitting quality. The physical compatibility between the assumed damage mechanism and the observed crack morphology should also be considered.

4. Conclusions

Creep tests performed at 575 °C under 310 MPa showed that the modified composition, involving simultaneous minor adjustments in nitrogen, boron, niobium, and carbon contents, was associated with a significant improvement in the creep life of 316L(N) stainless steel. Steel A exhibited a rupture life of 9203 h, compared with 649 h for the reference steel. The modified steel also showed higher elongation and necking values, 22.8% and 39.5%, respectively, compared with 18.8% and 29.5% for the reference steel. This indicates that the increase in rupture life was not accompanied by a loss of macroscopic ductility.

Microstructural observations revealed a clear difference in creep damage morphology. The reference steel developed elongated wedge-type cracks, whereas Steel A showed thicker and more rounded R-type cracks. This difference in morphology is consistent with the previously reported three-dimensional crack-thickness analysis, which showed finer crack features in the reference steel and thicker crack features in Steel A. Since N, Nb, B, and C were modified simultaneously, the observed difference in crack morphology should be interpreted as the result of combined minor compositional modifications rather than the effect of a single alloying element.

The primary and steady-state creep stages were described using the Estrin–Mecking framework. The fitted internal-stress parameters increased from 215 to 239 MPa for the reference steel and from 230 to 253 MPa for Steel A. These values should be interpreted as model-derived parameters rather than direct experimental measurements. The minimum creep rate also decreased from approximately $4\ x\ 10^{-5}\ h^{-1}$ in the reference steel to approximately $2\ x\ 10^{-6}\ h^{-1}$ in Steel A, which is consistent with the longer rupture life of the modified alloy.

The tertiary creep stage was analysed using the Ganesan damage-tolerance approach and Yin's cavity-growth model. The damage-tolerance parameter λ increased from 3.6 for the reference steel to 4.6 for Steel A, indicating a difference in the contribution of tertiary creep to the total deformation. The quantitative validation metrics showed that the Yin cavity-growth model provided the closest agreement with the experimental tertiary strain-rate evolution, with R^2 values of 0.902 for the reference steel and 0.900 for Steel A. However, the physical interpretation of the model parameters should still be considered together with the observed crack morphology. Yin's model is more directly compatible with wedge-type damage development, which was dominant in the reference steel, whereas Steel A mainly exhibited thicker and more rounded R-type cracks. This result suggests that crack morphology should be considered when interpreting tertiary creep model parameters, even when the alloys are compositionally close and tested under the same conditions.

5. Data Availability Statement

The datasets and calculation codes supporting this study, including the creep test results and model parameter files, are available from the corresponding author upon reasonable request.

6. Acknowledgments

The experimental datasets originate from the author's doctoral research and related previously published works, and are reinterpreted here through creep-stage modelling and damage-morphology-based discussion.

7. Authors Contributions

Oguz Berk Ozdemir is the sole author of this manuscript. The author was responsible for conceptualization, data interpretation, creep-stage modelling, manuscript preparation, and approval of the submitted version.

8. Conflict of interest

The author declares that there is no conflict of interest.

9. References

[1] AFCEN, RCC-MRx. Code-Design and construction rules for mechanical components of nuclear installations, Paris: AFCEN, 2018.

[2] F. Delabrouille, M. Blat-Yrieix and D. Buisine, "Nitrogen effect on creep properties of austenitic stainless steel," in *European Creep Collaborative Committee Conference*, Rome, Italy, 2014.

[3] M. Blat, F. Delabrouille, S. Goff and e. al., “EERA JPNM Task Force 60 years Operational Life Future Reactors,” European Energy Research Alliance (EERA), 2017.

[4] M. Blat-Yrieix, F. Delabrouille, C. Cabet, C. Petesch, G. Aiello and M. Blanc, “Important parameters to take into account to get reliable structural materials,” in *International Congress on Advances in Nuclear Power Plants (ICAP-2016)*, San Francisco, USA, 2016.

[5] O. Ozdemir, S. Valiyev, S. M. Montes, E. Ferrie, M. Blat-Yrieix, F. Delabrouille and L. Salvo, “Thermal ageing and creep damage in 316L (N) alloys: a 3D analysis.,” *Materials at High Temperatures,* pp. 1-9, 2022, https://doi.org/10.1080/09603409.2022.2058229.

[6] O. Ozdemir, L. Salvo, E. Ferrie and F. Delabrouille, “Creep behavior in austenitic stainless steel 316L(N): effects of minor element additions.,” *Materials at High Temperatures,* vol. 42, no. 1, pp. 68-77, 2025, https://doi.org/10.1080/09603409.2025.2461363.

[7] M. D. Mathew, G. Sasikala, K. B. Sankara Rao and S. L. Mannan, “Influence of carbon and nitrogen on the creep properties of type 316 stainless steel at 873 K,” *Materials Science and Engineering: A,* vol. 148, no. 2, pp. 253-260, 1991, https://doi.org/10.1016/0921-5093(91)90827-A.

[8] F. Abe, “Effect of boron on microstructure and creep strength ofadvanced ferritic power plant steels.,” *Procedia Engineering,,* vol. 10, pp. 94-99, 2011, https://doi.org/10.1016/j.proeng.2011.04.018.

[9] K. I. Hara, H. Aoki, F. Masuyama and T. Endo, “Effect of nitrogen on the high temperature creep behavior of 9cr-2Co steel.,” *ISIJ international,,* vol. 37(2), pp. 181-187, 1997, https://doi.org/10.2355/isijinternational.37.181.

[10] K. Kimura and K. Sawada, “Creep Deformation Property and Creep Life Evaluation of Super304H,” in *Volume 6: Materials and Fabrication*, Virtual, Online, 2020, https://doi.org/10.1115/PVP2020-21623.

[11] J. K. Solberg, “The influence of carbon and nitrogen on the high temperature creep properties of AISI Type 316 austenitic stainless steel,” *Materials Science and Engineering,* vol. 55, no. 1, pp. 39-44, 1982, https://doi.org/10.1016/0025-5416(82)90081-7..

[12] M. Fujiwara, H. Uchida and S. Ohta, “Effect of niobium content on creep strength of cold-worked 15Cr-15Ni-2.5 Mo austenitic steel.,” *Journal of materials science letters,* vol. 14.4, pp. 297-301, 1995, https://doi.org/10.1007/BF00275629.

[13] W. Jolly, C. Toffolon-Masclet, J. M. Joubert, B. Marini, F. Porcher, G. Andre and S. Ringeval, “In situ monitoring of isothermal phase transformation in two Nb stabilized austenitic stainless steels (316Nb) by neutron diffraction.,” *Journal of Alloys and Compounds,* vol. 688, pp. 695-702, 2016, https://doi.org/10.1016/j.jallcom.2016.07.244..

[14] V. Vodárek, G. Rožnovská and J. Sobotka, “Microstructure and creep properties of AISI 316LN steels with niobium additions,” *Materials Science Forum,* vol. 482, pp. 275-278, 2005, https://doi.org/10.4028/www.scientific.net/msf.482.275.

[15] A. Després, S. Antonov, C. Mayer, C. Tassin, M. Veron, J. J. Blandin and G. Martin, “On the role of boron, carbon and zirconium on hot cracking and creep resistance of an additively manufactured polycrystalline superalloy,” *Materialia,* vol. 101193, pp. 19,, 2021,https://doi.org/10.1016/j.mtla.2021.101193..

[16] M. Kurban and K. A. U. Erb, "A grain boundary characterization study of boron segregation and carbide precipitation in alloy 304 austenitic stainless steel," *Scripta Materialia,* vol. 54, no. 6, pp. 1053-1058, 2006, https://doi.org/10.1016/j.scriptamat.2005.11.055.

[17] K. Laha, J. Kyono, S. Kishimoto and N. Shinya, "Beneficial effect of B segregation on creep cavitation in a type 347 austenitic stainless steel," *Scripta Materialia,* vol. 52, no. 7, pp. 675-678, 2005, https://doi.org/10.1016/j.scriptamat.2004.11.016.

[18] J. H. Yoon, E. P. Yoon and B. S. Lee, "Correlation of chemistry, microstructure and ductile fracture behaviours of niobium-stabilized austenitic stainless steel at elevated temperature," *Scripta Materialia,* vol. 57, no. 1, pp. 25-28, 2007, https://doi.org/10.1016/j.scriptamat.2007.03.025.

[19] V. Ganesan, C. Praveen, J. Christopher, G. V. Prasad Reddy and M. Vasudevan, "Creep behavior of nuclear grade 316LN austenitic stainless steel at 873 K and 923 K.," *Mechanics of Time-Dependent Materials,* vol. 26, no. 3, pp. 593-610, 2022, https://doi.org/10.1007/s11043-021-09502-3.

[20] C. Praveen, J. Christopher, V. Ganesan, G. P. Reddy, G. Sasikala and S. K. Albert, "Constitutive modelling of transient and steady state creep behaviour of type 316LN austenitic stainless steel.," *Mechanics of Materials,* vol. 137, no. 103122, 2019, https://doi.org/10.1016/j.mechmat.2019.103122..

[21] C. Praveen, J. Christopher, V. Ganesan, G. P. Reddy and S. K. Albert, "Influence of varying nitrogen on creep deformation behaviour of 316LN austenitic stainless steel in the framework of the state-variable approach," *Materials Science and Engine,* vol. 803, 2021, https://doi.org/10.1016/j.msea.2020.140503.

[22] Y. F. Yin and R. G. Faulkner, "Continuum damage mechanics modelling based on simulations of microstructural evolution kinetics.," *Materials science and technology,* vol. 22, no. 8, pp. 929-936, 2006, https://doi.org/10.1179/174328406X102426.

[23] Y. Cui, M. Sauzay, C. Caes, P. Bonnaillie, B. Arnal, C. Cabet, M. Blat-Yrieix and S. Dubiez-Legoff., "Modeling and experimental study of long term creep damage in austenitic stainless steels," *Engineering Failure Analysis,* Vols. Volume 58, Part 2, pp. 452-464, 2015, https://doi.org/10.1016/j.engfailanal.2015.08.009.

[24] Y. Estrin and H. Mecking, "A unified phenomenological description of work hardening and creep based on one-parameter models," *Acta Metallurgica,* vol. 32, no. 1, pp. 57-70, 1984, https://doi.org/10.1016/0001-6160(84)90202-5.

[25] M. Ashby and B. Dyson, "Creep damage mechanics and micromechanisms," *Fracture,* vol. 84, pp. 3-30, 1984, https://doi.org/10.1016/B978-1-4832-8440-8.50017-X.

[26] M. B. Bettaieb, A. Renault-Laborne, S. Depinoy, L. Vincent and T. Morgeneyer, "Effect of microstructure on creep mechanical behavior and damage mechanisms of AISI 316L (N) austenitic stainless steels," *Procedia Structural Integrity,* 2025, https://doi.org/10.1016/j.prostr.2025.06.057.

[27] R. Mersereau and A. V. Oppenheim, "Digital reconstruction of multidimensional signals from their projections," *in Proceedings of the IEEE,* vol. 62, no. 10, pp. 1319-1338, 1974, doi:10.1109/PROC.1974.9625.